



OPEN

Enhancing Li-ion battery anode performances via $\text{Li}_{1.5}\text{Al}_{0.5}\text{Ti}_{1.5}(\text{PO}_4)_3$ coated $\text{Li}_{1.2}\text{Mn}_{0.54}\text{Ni}_{0.13}\text{Co}_{0.13}\text{O}_2$ cathode

Shang-Mei Yang, Shi-Ping Shao & Yu-Long Xie✉

The material $\text{Li}_{1.5}\text{Al}_{0.5}\text{Ti}_{1.5}(\text{PO}_4)_3$ is a lithium fast ion conductor with three-dimensional ion channels. It exhibits high ionic conductivity, with lithium ion conductivity. To prevent long-term direct contact between $\text{Li}_{1.2}\text{Mn}_{0.54}\text{Ni}_{0.13}\text{Co}_{0.13}\text{O}_2$ material and electrolyte, and avoid HF corrosion of the electrode produced by the decomposition of the electrolyte. A three-dimensional skeleton lithium fast ion conductor $\text{Li}_{1.5}\text{Al}_{0.5}\text{Ti}_{1.5}(\text{PO}_4)_3$ coating layer was successfully synthesized on the surface of the lithium-rich manganese-based positive electrode material $\text{Li}_{1.2}\text{Mn}_{0.54}\text{Ni}_{0.13}\text{Co}_{0.13}\text{O}_2$. The experimental results show that the $\text{Li}_{1.2}\text{Mn}_{0.54}\text{Ni}_{0.13}\text{Co}_{0.13}\text{O}_2@\text{Li}_{1.5}\text{Al}_{0.5}\text{Ti}_{1.5}(\text{PO}_4)_3$ composite material with a coating amount of 3% has the highest capacity retention rate after 100 cycles. The capacity retention rate reaches 85.9% after 100 cycles at 0.1 C, which is better than the 82.14% of the base material. It proves that the $\text{Li}_{1.5}\text{Al}_{0.5}\text{Ti}_{1.5}(\text{PO}_4)_3$ coating layer effectively prevents the occurrence of side reactions during long cycles, stabilizes the electrode surface structure, and reduces capacity loss.

Keywords Coating materials, Sol-gel processes, Diffusion, $\text{Li}_{1.5}\text{Al}_{0.5}\text{Ti}_{1.5}(\text{PO}_4)_3$

In recent decades, due to the effective utilization of renewable energy, lithium-ion batteries (LiBs) have become widely used as energy storage power supplies for hydropower, wind power, solar power stations, and small electric vehicles, owing to their large capacity. In addition, they have also demonstrated promising development prospects in various military equipment, aerospace, satellites, and space stations, among other fields¹. The commercialization of lithium-ion batteries has mitigated carbon dioxide greenhouse gas emissions and reduced the high demand for fossil fuels². However, despite the numerous advantages of lithium-ion batteries, there are still certain challenges and limitations associated with their use. First of all, the safety of lithium-ion batteries has garnered significant attention, particularly in extreme conditions such as high temperatures, overcharging, or external damage. These conditions can lead to thermal runaway, explosions, and other safety issues³. Secondly, lithium-ion batteries still require improvement in cycle life and energy density to meet the growing demand for high-performance batteries for electric vehicles and energy storage systems. Additionally, the limited rare metal resources in lithium-ion batteries, as well as the environmental and resource pressures in their manufacturing and recycling processes, present significant challenges⁴. The main reason for this underperformance is the development of electrode materials^{5,6}. Currently, the primary anode material used in the commercial production of lithium-ion batteries is mainly carbon. The specific capacity of this material can typically be stabilized at 350 mAh·g⁻¹ or more. However, the specific capacity of the corresponding commercial anode material is less than 200 mAh·g⁻¹, significantly hindering the development of lithium-ion batteries.

The lithium rich manganese-based oxide $\text{Li}_{1.2}\text{Mn}_{0.54}\text{Ni}_{0.13}\text{Co}_{0.13}\text{O}_2$ has a reversible specific capacity of more than 250 mAh·g⁻¹ and a high working voltage (> 3.5 V vs. Li/Li⁺). It also has the characteristics of being cost-effective and plays an important role in portable electronic devices. Furthermore, it is considered as an ideal power source for next-generation hybrid electric vehicles (HEVs) and electric vehicles (EVs), and is a promising anode material⁷. During the charging and discharging of batteries, there are issues with poor cycle stability, significant voltage drop, initial capacity loss, and reduced performance caused by manganese atom migration and oxygen release, leading to an irreversible phase transition that hinders its application^{8–10}. Therefore, current research is focused on improving the retention rate and lifespan of batteries. Surface coating is often used to alter the surface of battery active materials. It acts as a physical barrier and creates a stable CEI film during

School of Chemistry and Materials Science, Key Laboratory of Resource Chemistry and Eco-environmental Protection in Tibetan Plateau of State Ethnic Affairs Commission, Qinghai Provincial Key Laboratory of Nanomaterials and Nanotechnology, Qinghai Minzu University, Xining 810007, China. ✉email: yulongxie2012@126.com

charge and discharge cycles. This helps prevent side reactions between the electrode surface and the electrolyte by slowing down the decomposition of the electrolyte and maintaining the oxidation ion vacancy in the lattice. As a result, it enhances the surface stability of the coating material, significantly improving the initial discharge capacity and capacity retention throughout the cycle^{11–13}. In recent years, researchers have utilized various surface coating materials, including SmPO_4 ¹⁴, amorphous boron phosphate glass (combined)¹⁵, epoxy silane¹⁶, TiO_2 ¹⁷, ZrO_2 ¹⁸, $\text{AlF}_3\text{-Al}_2\text{O}_3$ ¹⁹, and other materials^{11,12}, to coat $\text{Li}_{1.2}\text{Mn}_{0.54}\text{Ni}_{0.13}\text{Co}_{0.13}\text{O}_2$. This coating aims to enhance the electrochemical performance of Li-rich cathode materials. However, most metal oxides are not lithium-ion conductors, which can result in high interface resistance between the cathode and the electrolyte. Surface modification with lithium-ion conductors offers unique advantages in this regard²⁰.

The material $\text{Li}_{1.5}\text{Al}_{0.5}\text{Ti}_{1.5}(\text{PO}_4)_3$, also known as a Na Super Ion Conductor (NASICON), is a lithium fast ion conductor with three-dimensional ion channels. It exhibits high ionic conductivity, with lithium ion conductivity of 10^{-3} $\text{S}\cdot\text{cm}^{-1}$ ²¹. This material is considered a good solid electrolyte for high-energy batteries and is favored by researchers due to its excellent ion transport performance and chemical stability²². $\text{Li}_{1.5}\text{Al}_{0.5}\text{Ti}_{1.5}(\text{PO}_4)_3$ has a high lithium ion diffusion coefficient and good electrochemical stability, which can effectively reduce the polarization effect and improve the battery's cycle life. However, its low conductivity makes it unsuitable for direct use in the electrode, as this would decrease battery performance. To address this issue, researchers have proposed using $\text{Li}_{1.5}\text{Al}_{0.5}\text{Ti}_{1.5}(\text{PO}_4)_3$ as a surface coating material for modifying the cathode materials of lithium-ion batteries in recent years. Choi et al.²³ applied a NASICON-type lithium conductor $\text{Li}_{1.3}\text{Al}_{0.3}\text{Ti}_{1.7}(\text{PO}_4)_3$ (LATP) coating on C622 using a single gel process to address the limitations of C622. The study revealed that applying 0.5 wt% LATP on the surface of C622 substantially enhances battery performance, including discharge capacity, rate capacity, and cycle stability. However, the overall battery performance decreases with an increase in the coating amount beyond 1.0 wt%. Electrochemical analysis indicates that the improved battery performance is due to a high lithium ion diffusion coefficient and low interfacial resistance. Excessive coating, on the other hand, may hinder the movement of lithium ions and reduce battery performance. Liang et al.²⁴ utilized $\text{Li}_{1.4}\text{Al}_{0.4}\text{Ti}_{1.6}(\text{PO}_4)_3$ as the model cathode and applied a coating of $\text{Li}_{1.4}\text{Al}_{0.4}\text{Ti}_{1.6}(\text{PO}_4)_3$ onto the surface of $\text{LiNi}_{0.6}\text{Co}_{0.2}\text{Mn}_{0.2}\text{O}_2$. This was done to reduce polarization and improve dynamic characteristics. The researchers investigated the key properties of this improved kinetics using atomic force microscopy and boundary potential analysis. The results showed that the formed interfacial transition layer provides a gradual potential slope and sustained polarization, resulting in improved cycle stability at room temperature (90% capacity retention after 100 cycles) and excellent rate capability (116 $\text{mAh}\cdot\text{g}^{-1}$ at 2 °C). In a study by Wu et al.²⁵, LiMn_2O_4 particles were coated with $\text{Li}_{1.3}\text{Al}_{0.3}\text{Ti}_{1.7}(\text{PO}_4)_3$ using a wet chemical method. It was observed that the corners and edges of the coated LiMn_2O_4 particles were not as distinct as those without coating. The study found that the lithium-ion diffusion coefficients of the two powders are similar. However, at room temperature and 55 °C, the capacity retention rates of $\text{Li}_{1.3}\text{Al}_{0.3}\text{Ti}_{1.7}(\text{PO}_4)_3$ -coated LiMn_2O_4 were 98.2% and 93.9%, respectively, which were significantly higher than those of uncoated LiMn_2O_4 at 85.4% and 79.1%. As the charge and discharge ratio increased, the capacity retention difference between $\text{Li}_{1.3}\text{Al}_{0.3}\text{Ti}_{1.7}(\text{PO}_4)_3$ -coated LiMn_2O_4 and uncoated LiMn_2O_4 also increased at both room temperature and 55 °C, with the capacity retention rate of coated LiMn_2O_4 being 8.4% higher than that of uncoated LiMn_2O_4 at room temperature and 11.1% higher at 55 °C. Wang et al.²⁶ utilized mechanical fusion to alter the surface of the lithium-ion conductors $\text{Li}_{1.4}\text{Al}_{0.4}\text{Ti}_{1.6}(\text{PO}_4)_3$ and $\text{Li}(\text{Ni}_{0.6}\text{Co}_{0.2}\text{Mn}_{0.2})\text{O}_2$. After 100 cycles, the capacity retention rate was 90.9%, significantly higher than that of the unmodified material (79%). Additionally, the $\text{Li}_{1.4}\text{Al}_{0.4}\text{Ti}_{1.6}(\text{PO}_4)_3$ coating also enhances the rate performance and thermal stability of the material. The improved performance can be attributed to the enhanced stability of the interface between $\text{Li}(\text{Ni}_{0.6}\text{Co}_{0.2}\text{Mn}_{0.2})\text{O}_2$ and electrolyte through the modification of $\text{Li}_{1.4}\text{Al}_{0.4}\text{Ti}_{1.6}(\text{PO}_4)_3$. These results offer a potential method for developing dependable cathode materials with high energy density and long cycle life.

In this study, a sol-gel method was used to synthesize composite materials of $\text{Li}_{1.2}\text{Ni}_{0.13}\text{Co}_{0.13}\text{Mn}_{0.54}\text{O}_2@ \text{Li}_{1.5}\text{Al}_{0.5}\text{Ti}_{1.5}(\text{PO}_4)_3$. The electrochemical behavior of the material with the optimum coating ratio in the battery was examined through relevant characterization and electrochemical performance tests.

Materials and methods

Synthesis of the pristine and $\text{Li}_{1.5}\text{Al}_{0.5}\text{Ti}_{1.5}(\text{PO}_4)_3$ coated material

The original layered oxide $\text{Li}_{1.2}\text{Mn}_{0.54}\text{Ni}_{0.13}\text{Co}_{0.13}\text{O}_2$ (LNCM) powder was prepared using the sol-gel method followed by high-temperature combustion, which employs a similar approach as previously reported²⁷. In the preparation of $\text{Li}_{1.2}\text{Mn}_{0.54}\text{Ni}_{0.13}\text{Co}_{0.13}\text{O}_2@ \text{Li}_{1.5}\text{Al}_{0.5}\text{Ti}_{1.5}(\text{PO}_4)_3$ materials, first take 1.3412 mL of tetrabutyl titanate dissolved in 14 mL anhydrous ethanol and ultrasonicate for 30 min. At the same time, 0.4927 g $\text{AlNO}_3\cdot 9\text{H}_2\text{O}$ and 0.4020 g $\text{CH}_3\text{COOLi}\cdot 2\text{H}_2\text{O}$ were respectively dissolved into 10 mL deionized water and stirred for 10 min to fully dissolve them. Then weigh 0.5520 g citric acid and dissolve it in 5 mL deionized water, weigh 0.9065 g $\text{NH}_4\text{H}_2\text{PO}_4$ and dissolve it in 3 mL deionized water, stirring for 10 min. Then 8 mL of glacial acetic acid was slowly dropped into the ethanol solution of the ultrasonic tetrabutyl titanate, and stirred for 20 min to inhibit the hydrolysis of tetrabutyl titanate. Finally, citric acid aqueous solution and $\text{NH}_4\text{H}_2\text{PO}_4$ aqueous solution were added to the above solution and stirred for 10 min respectively to obtain a milky 0.025 g·mL⁻¹ $\text{Li}_{1.5}\text{Al}_{0.5}\text{Ti}_{1.5}(\text{PO}_4)_3$ solution in a fixed volume to 100 mL volume bottle. 0.00025 g·mL⁻¹ $\text{Li}_{1.5}\text{Al}_{0.5}\text{Ti}_{1.5}(\text{PO}_4)_3$ solution was obtained for use.

Weigh and disperse 0.1 g of LNCM powder into a 20 mL aqueous solution containing $\text{Li}_{1.5}\text{Al}_{0.5}\text{Ti}_{1.5}(\text{PO}_4)_3$. Stir the mixture at a constant temperature and speed in a water bath at 85 °C until all the solvent evaporates, leaving behind a dry black powder. Dry the powder for 4 h at 120 °C, then place it in a tube furnace in an air atmosphere and sinter it at 800 °C for 6 h. This process will result in a surface cladding layer of $\text{Li}_{1.5}\text{Al}_{0.5}\text{Ti}_{1.5}(\text{PO}_4)_3$ on the $\text{Li}_{1.2}\text{Ni}_{0.13}\text{Co}_{0.13}\text{Mn}_{0.54}\text{O}_2$. The content of $\text{Li}_{1.5}\text{Al}_{0.5}\text{Ti}_{1.5}(\text{PO}_4)_3$ coating ranged from 0 to 4 wt% of the LNCM powder, denoted as LATP-05-0, LATP-05-1, LATP-05-1.5, LATP-05-2, LATP-05-3, and LATP-05-4, respectively.

Materials characterization

The crystalline structure of LNCM and $\text{Li}_{1.5}\text{Al}_{0.5}\text{Ti}_{1.5}(\text{PO}_4)_3$ was analyzed using powder X-ray diffraction (XRD), utilizing Cu-K α radiation. Scans were conducted within the range of 10 to 90 degrees at a rate of 10 $^{\circ}\text{min}^{-1}$. Scanning electron microscopy (SEM; GeminiSEM300) was used to visually observe the surface morphology of the sample. During the test, the sample was secured onto the metal sample table using conductive tape. An accelerated voltage of 5 kV was applied, enabling the rough determination of the sample particle size. For further analysis of morphology, particle size, and microstructure, Transmission electron microscopy (TEM; The JEM-2100, Japan) was employed. The TEM specifications include a point resolution of 0.23 nm, lattice resolution of 0.14 nm, acceleration voltage range of 80–200 kV, and magnification range of 50–1,500,000. X-ray Photoelectron Spectroscopy (XPS) utilizes X-ray radiation to excite and emit valence or inner electrons of atoms or molecules. This technique allows for the detection of elements with atomic numbers equal to or greater than 3. XPS finds significant application in the characterization of lithium-ion battery cathode materials. It primarily serves to measure the types and valence states of elements on the surface of materials. In this paper, Thermo Field ESCALAB 250Xi X-ray photoelectron spectrometer is used for testing. The excitation light source uses Al-K α ray, the energy is 1486.6 eV, the working voltage is 14.6 kV, and the vacuum degree of the analysis chamber is 4×10^{-9} mbar. The standard is calibrated by C 1s = 284.8 eV.

Electrochemical measurement

Material electrochemical characterization was conducted through CR2032 coin cell tests. The cathode electrodes were fabricated using a composition comprising cathode powder, Super P, and PVDF (mass ratio of 8:1:1) dissolved in N-methyl-2-pyrrolidone (NMP). Following thorough mixing, the slurry was uniformly spread onto an aluminum foil using a notch bar spreader with a thickness of 100 μm . It was then underwent drying at 120° C for 12 h within a vacuum oven. After compression at 10 MPa for 1 min, the resulting electrode was then cut into circular plates measuring 14 mm in diameter. All CR2032 coin cells were assembled within an argon-filled glovebox (H_2O , $\text{O}_2 < 0.1$ ppm), employing lithium metal as the anode. LiPF_6 (1 M) was dissolved in a mixture of ethylene carbonate and ethyl methyl carbonate (3:7 weight ratio) and a 25 μm trilayer polypropylene-polyethylene-polypropylene membrane (MTI) were used as the electrolyte and separator, respectively. The electrochemical performance was assessed utilizing a land battery testing system (LAND CT2001A). Charging and discharging of all cells were conducted at ambient temperature, within a potential range spanning from 2.0 to 4.8 V versus Li/Li^+ . The electrochemical workstation, CHI660B, facilitated the Electrochemical Impedance Spectroscopy (EIS) and cyclic voltammetry (CV) tests for the cells. EIS testing parameters comprised a 10 mV amplitude and a frequency range spanning from 10 MHz to 100 kHz. Meanwhile, CV parameters entailed a voltage range from 2.0 to 4.8 V and a scanning rate of 0.1 $\text{mV}\cdot\text{s}^{-1}$.

Result and discussion

In order to obtain the crystal structure characteristics of the material, the sample was subjected to X-ray powder diffraction analysis. Figure 1 shows the XRD spectra of the obtained LNCM sample LATP-05-X ($X = 0, 1, 1.5, 2, 3, 4$) and $\text{Li}_{1.5}\text{Al}_{0.5}\text{Ti}_{1.5}(\text{PO}_4)_3$ positive electrode material. Figure 1(a) is a comparison of the XRD spectra of the six samples LATP-05-X ($X = 0, 1, 1.5, 2, 3, 4$). All synthetic materials show a high-intensity diffraction peak with the R-3 m space group, and the low-intensity diffraction peak between 20° and 25° represents the monoclinic phase Li_2MnO_3 with the C2/m space group, which belongs to the typical hexagonal layered $\alpha\text{-NaFeO}_2$ structure. The characteristic peaks of the $\text{Li}_{1.2}\text{Mn}_{0.54}\text{Ni}_{0.13}\text{Co}_{0.13}\text{O}_2$ cathode materials before and after coating modification in six different ratios remain basically consistent, indicating that the lithium fast ion conductor $\text{Li}_{1.5}\text{Al}_{0.5}\text{Ti}_{1.5}(\text{PO}_4)_3$ coated on the surface of the cathode material has not changed the internal structure of the raw material. The peak splits of the crystal planes (006)/(102) and (108)/(110) are more obvious, indicating that all materials have good layered structures.

To gain deeper insights into the internal crystal structure of the fast Li-ion conductor $\text{Li}_{1.5}\text{Al}_{0.5}\text{Ti}_{1.5}(\text{PO}_4)_3$ (LATP) before and after coating and modification, Table 1 lists the lattice parameters obtained from Rietveld refinement using the GSAS-II software, and the refinement results are shown in Figure S1. The data in the table

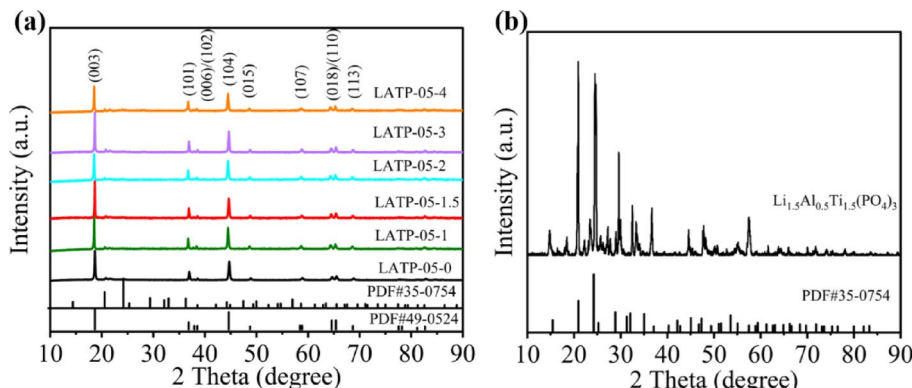
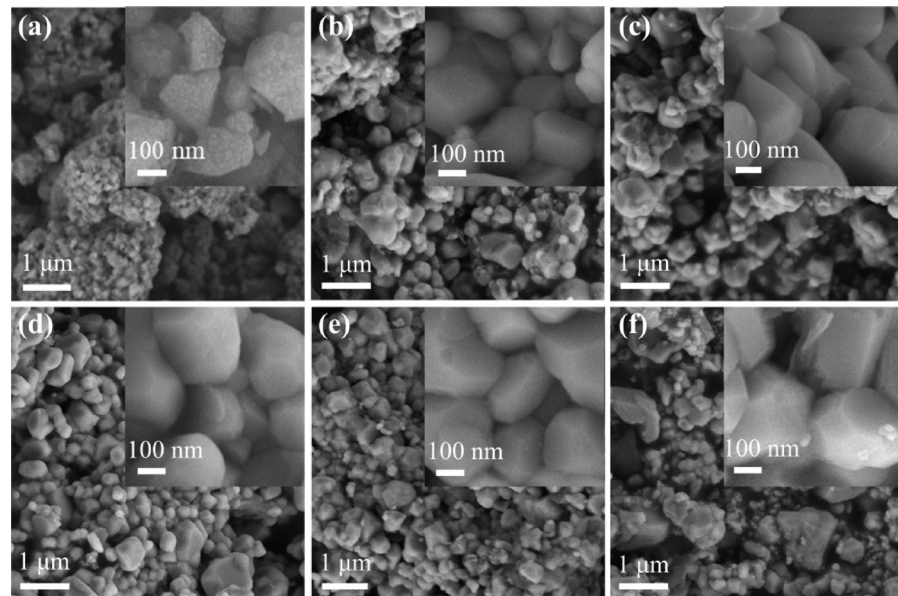


Fig. 1. XRD spectra of (a) LATP-05-X ($X = 0, 1, 2, 3, 4$) and (b) $\text{Li}_{1.5}\text{Al}_{0.5}\text{Ti}_{1.5}(\text{PO}_4)_3$.

Sample	a/(nm)	c/(nm)	c/a	$I_{(003)}/I_{(104)}$
LATP-05-0	2.8556	14.2605	4.9939	1.5267
LATP-05-1	2.8580	14.2569	4.9884	1.4409
LATP-05-1.5	2.8573	14.2564	4.9895	1.7668
LATP-05-2	2.8572	14.2600	4.9909	1.2804
LATP-05-3	2.8568	14.2675	4.9943	1.8416
LATP-05-4	2.8581	14.2743	4.9943	1.4599

Table 1. Lattice parameters of LATP-05-X (X=0, 1, 1.5, 2, 3, 4).**Fig. 2.** (a-f) SEM images of LATP-05-X (X=0, 1, 1.5, 2, 3, 4).

show that the c/a values in the lattice of the material LATP-05-X (X=0, 1, 1.5, 2, 3, 4) are all over 4.9, and the materials are all perfect cubic close-packed structures. Among them, the c/a value (4.9943) and $I_{(003)}/I_{(104)}$ ratio (1.8416) of the LATP-05-3 material are both the largest, indicating that the internal space of the LATP-05-3 material is the largest, and the mixing degree of cations is the lowest. The lithium ion deintercalation channel is wide, which is conducive to the deintercalation of lithium ions, and then improves the electrochemical performance of the material. No obvious P, Ti, and Al element peaks were observed in the XRD spectrum, which may be due to the small coating amount and low element content. In order to verify the synthesis of $\text{Li}_{1.5}\text{Al}_{0.5}\text{Ti}_{1.5}(\text{PO}_4)_3$ phase on the LNCM surface, XRD analysis was performed on the pure coating material synthesized under the same conditions, and the results are shown in Fig. 1(b). Compared with the standard PDF card of $\text{Li}_{1.5}\text{Al}_{0.5}\text{Ti}_{1.5}(\text{PO}_4)_3$ in the database, most of the peaks of the synthesized $\text{Li}_{1.5}\text{Al}_{0.5}\text{Ti}_{1.5}(\text{PO}_4)_3$ phase are basically consistent with the standard, verifying the formation of $\text{Li}_{1.5}\text{Al}_{0.5}\text{Ti}_{1.5}(\text{PO}_4)_3$ under the synthesis conditions.

The morphology of these materials was observed by scanning electron microscopy, as shown in Fig. 2. From Fig. 2(a) to (f), the morphology of all samples is irregular small particles without obvious large-area aggregation. In addition, the morphology of LNCM remains basically unchanged before and after coating modification, indicating that the presence of $\text{Li}_{1.5}\text{Al}_{0.5}\text{Ti}_{1.5}(\text{PO}_4)_3$ has no significant effect on particle growth. From LATP-05-0 to LATP-05-3, the dispersion of sample particles gradually improves, among which LATP-05-3 has the most uniform particle dispersion, and the smaller particle size is conducive to the enhancement of electrochemical performance. LATP-05-4 shows slight agglomeration, which may be due to the rough surface of the material caused by excessive coating.

Figure 3 (a-f) is the EDS mapping of sample LATP-05-3 at 20 μm. It can be observed from the figure that Ni, Co, Mn, Al, Ti and P are evenly distributed on the LNCM surface.

Table 2 lists the element percentage distribution of Ni, Mn, Co, Ti, P, and Al in turn. The element percentage distribution corresponds to the stoichiometric ratio of the LATP-05-3 material, confirming the coating of $\text{Li}_{1.5}\text{Al}_{0.5}\text{Ti}_{1.5}(\text{PO}_4)_3$ on the surface of the lithium-rich manganese-based positive electrode material.

The TEM image of the LATP-05-3 sample is shown in Fig. 4. Figure 4(a) clearly shows that the material has a clear boundary, and a layer of gray material is wrapped around the black main material. The green area in Fig. 4(a) is selected to analyze the internal lattice of the main material at a higher magnification, as shown in Fig. 4(b).

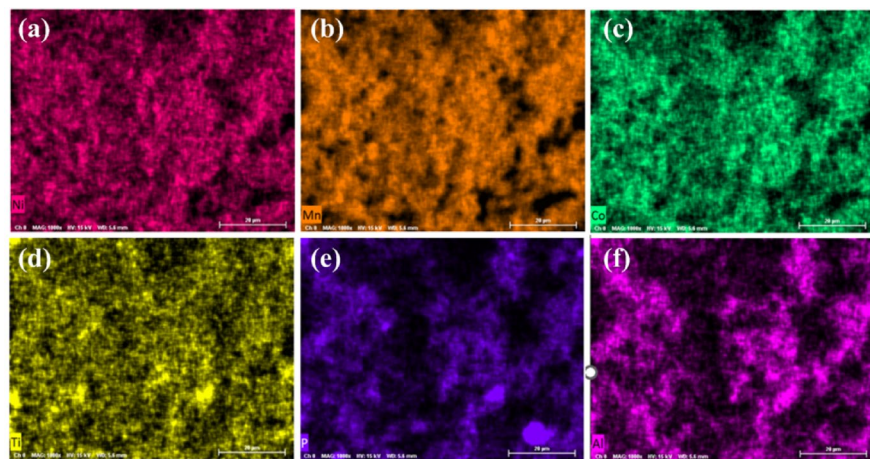


Fig. 3. (a-f) Elemental mapping of LATP-05-3 via EDS.

Element	Mass (%)	Atom (%)
Mn	63.24	63.17
Co	17.1	15.92
Ni	16.28	15.22
Al	0.97	1.98
Ti	0.87	0.99
P	1.54	2.72
Total	100.00	100.00

Table 2. The element content rates of mn, co, ni, al, Ti and P as per the EDS mapping results.

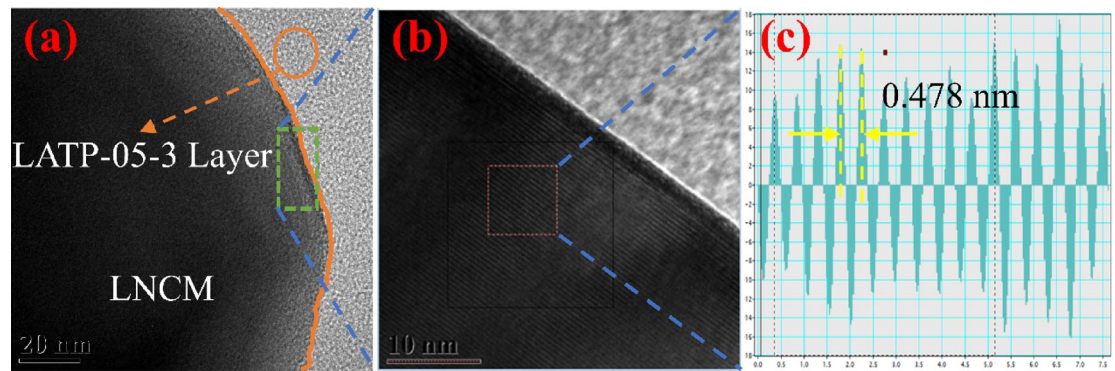


Fig. 4. TEM image of LATP-05-3.

Figure 4(c) Fourier transform shows that the lattice spacing of the material is 0.478 nm, corresponding to the (003) crystal plane of LNCM. Combined with the element content information in EDS, it can be determined that the gray coating is $\text{Li}_{1.5}\text{Al}_{0.5}\text{Ti}_{1.5}(\text{PO}_4)_3$, which is consistent with the XRD results.

In order to further explore the relationship between material particle size and performance, the uncoated positive electrode material $\text{Li}_{1.2}\text{Mn}_{0.54}\text{Ni}_{0.13}\text{Co}_{0.13}\text{O}_2$ and the material coated with $\text{Li}_{1.5}\text{Al}_{0.5}\text{Ti}_{1.5}(\text{PO}_4)_3$ were analyzed for particle size. For each material, 100 groups of particles were selected from the scanning electron microscope images at the same magnification. As can be seen from Fig. 5, the material particle size is mainly distributed between 0.1 and 1.5 μm . In Fig. 5(a), the average particle size of the uncoated positive electrode material LNCM particles is about 0.3 μm , and the normal distribution curve also shows the smallest degree of discreteness. This is because the uncoated positive electrode material has agglomeration compared to the coated modified material. Figure 5(b-f) are the particle size distribution diagrams of LATP-05-1, LATP-05-1.5, LATP-05-2, LATP-05-3, and LATP-05-4, respectively. It can be seen from the figure that the average particle size of all materials after coating and modification remains between 0.46 and 0.51 μm , and the sample particles

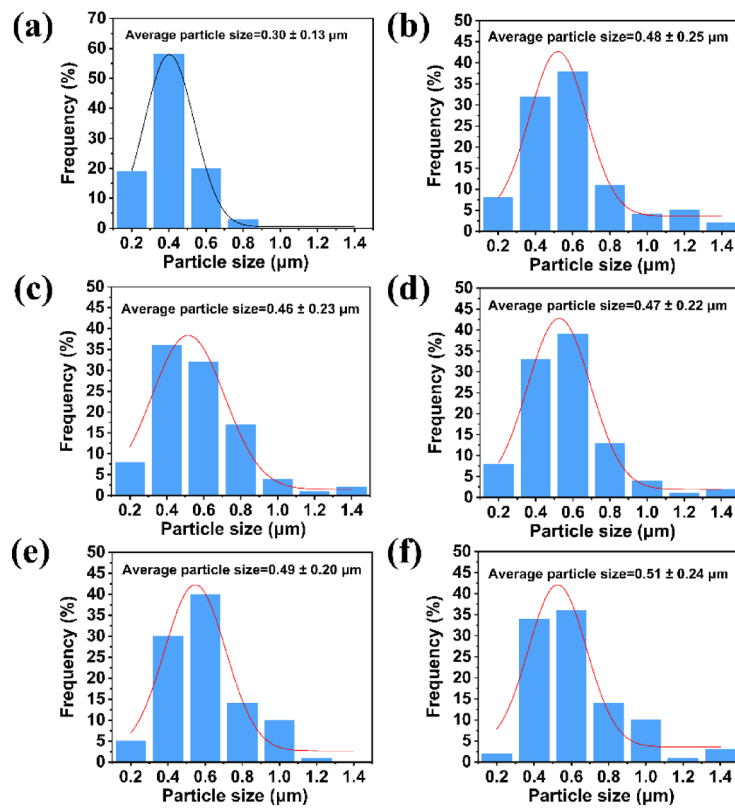


Fig. 5. Particle size distribution of LATP-05-X (X = 0, 1, 1.5, 2, 3, 4).

are relatively evenly dispersed. Among them, the normal distribution curve of LATP-05-3 material shows the smallest degree of discreteness, indicating that the sample particle size is the most uniform. In the process of participating in the electrochemical reaction, it can effectively accelerate the lithium ion deintercalation rate, thereby improving the electrochemical performance.

In order to obtain the valence distribution of elements in the lithium-rich manganese-based cathode material coated with $\text{Li}_{1.5}\text{Al}_{0.5}\text{Ti}_{1.5}(\text{PO}_4)_3$, the LATP-05-3 material was tested by XPS, and the binding energy of the measured elements was calibrated with the external carbon source C 1s (284.8 eV). Figure 6(a-c) are the fine spectrum comparisons of Ni 2p, Co 2p, and Mn 2p in LATP-05-0 and LATP-05-3 materials, respectively. The element spectra before and after $\text{Li}_{1.5}\text{Al}_{0.5}\text{Ti}_{1.5}(\text{PO}_4)_3$ coating are basically the same. The main peak of Ni 2p3/2 orbital binding energy is located at 855.68 eV, and the satellite peak is located at 861.98 eV; while the main peak of Ni 2p1/2 orbital binding energy is located at 872.7 eV, and the satellite peak is located at 879.78 eV, with a split energy level difference of $\Delta E = 17.02$ eV, indicating that the Ni element in the sample before and after coating modification is +2 valence. Analyzing the position of the 2p orbital split peak binding energy of Co, the orbital binding energy of Co 2p3/2 is 780.98 eV, while the orbital binding energy of Co 2p1/2 is 795.88 eV, with a split energy level difference of $\Delta E = 14.9$ eV, indicating that the Co element in the sample is +3 valence. The Mn 2p orbital presents two main peaks, Mn 2p3/2 at 642.98 eV and Mn 2p1/2 at 654.58 eV, respectively, without corresponding satellite peaks, and the binding energy position corresponds to Mn^{4+} . Figure 6(d-f) are the fine spectra of Ti 2p, P 2p, and Al 2p in the LATP-05-3 material. The Ti 2p3/2 orbital binding energy is at 458.58 eV, and the Ti 2p1/2 orbital binding energy is at 464.18 eV, proving the presence of Ti^{4+} in the material; the P 2p binding energy is at 133.38 eV, indicating that P exists on the surface of the $\text{Li}_{1.5}\text{Al}_{0.5}\text{Ti}_{1.5}(\text{PO}_4)_3$ coating sample; the Al 2p3/2 orbital binding energy is at 72.58 eV, indicating the presence of Al^{3+} . XPS analysis proves that Ni is +2 valence, Co and Al are +3 valence, and Mn and Ti are +4 valence in the lithium-rich manganese-based positive electrode material before and after $\text{Li}_{1.5}\text{Al}_{0.5}\text{Ti}_{1.5}(\text{PO}_4)_3$ coating.

In order to better demonstrate the performance of LATP-05-3 materials, electrochemical performance tests were carried out. Figure 7(a) is the first charge and discharge curve of LATP-05-X (X = 0, 1, 1.5, 2, 3, 4) materials at room temperature (25 °C), voltage range 2.0 ~ 4.8 V, and current density of 0.1 C. All electrodes show the electrochemical characteristics of two voltage platforms typical of lithium-rich manganese-based materials, and no new contours appear on the surface of the coated and modified electrode, indicating that the surface coating does not participate in the electrochemical process. The tilted area below 4.5 V corresponds to the migration of Li^+ and the oxygen of low-valent transition metals in the LiTMO_2 component; the platform above 4.5 V belongs to the activation of the Li_2MnO_3 component. Comparing the initial charge and discharge curves of the six samples, it was found that the initial discharge capacity of the coated LATP-05-1.5 sample was the highest, reaching 219 $\text{mAh}\cdot\text{g}^{-1}$, and the initial Coulomb efficiency (71.29%) was also higher than that of the uncoated LATP-05-0 sample (51.22%), showing the best charge and discharge performance among the six materials. Subsequently, the

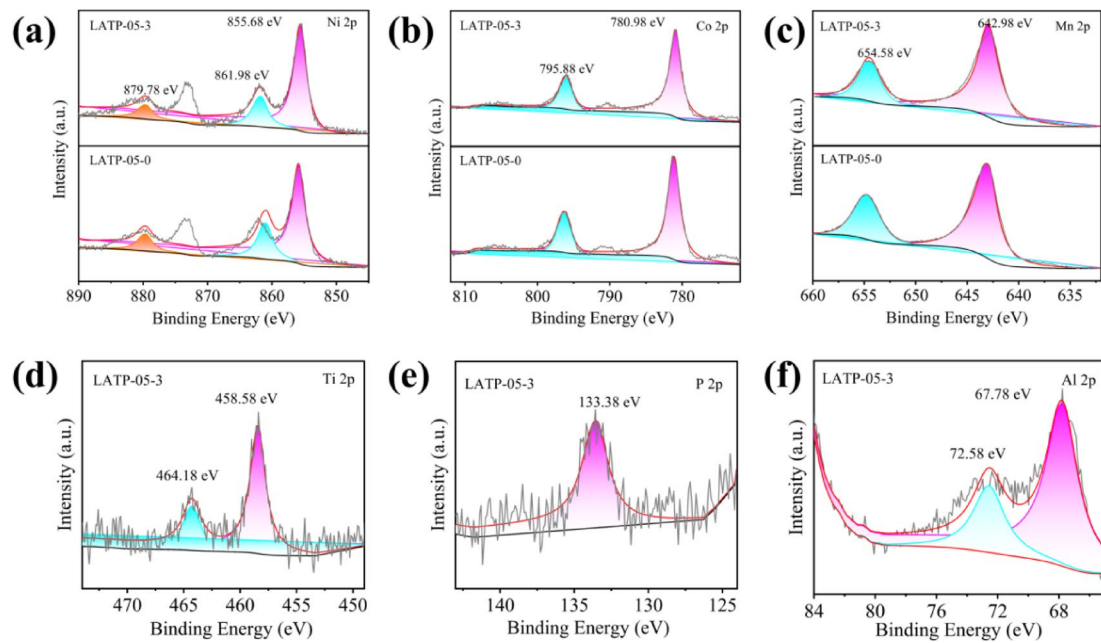


Fig. 6. Comparison of XPS spectra of LATP-05-0 and LATP-05-3 (a-c) Ni 2p、Co 2p、Mn 2p; (d) Ti 2p spectrum (e) P 2p spectrum; (f) Al 2p spectrum.

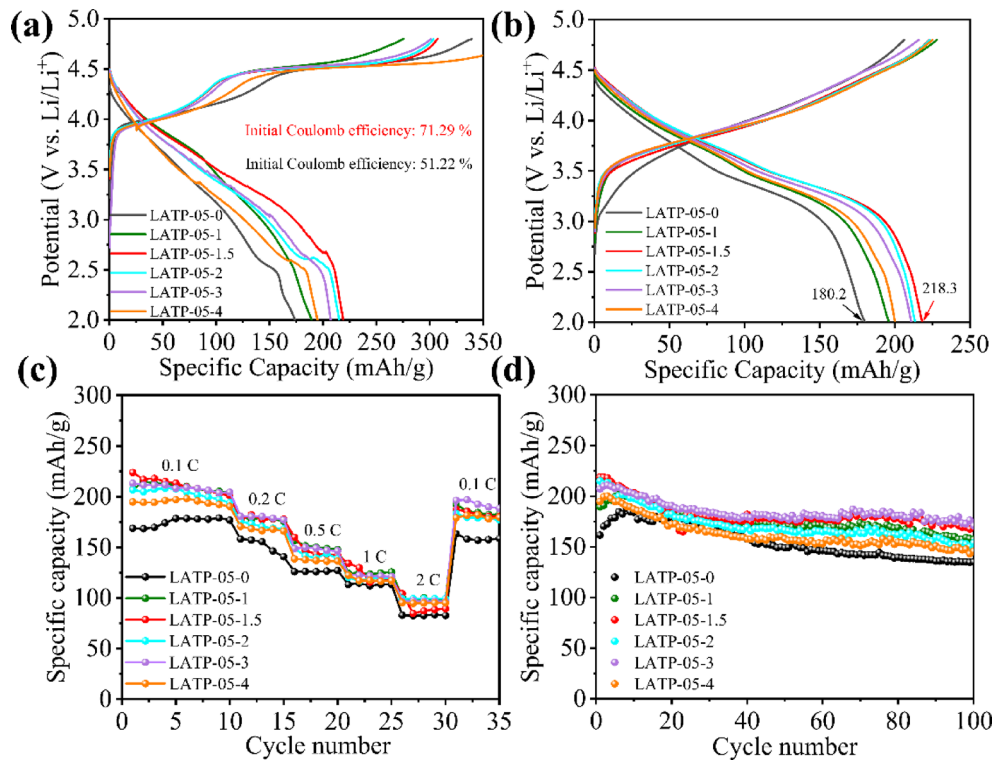
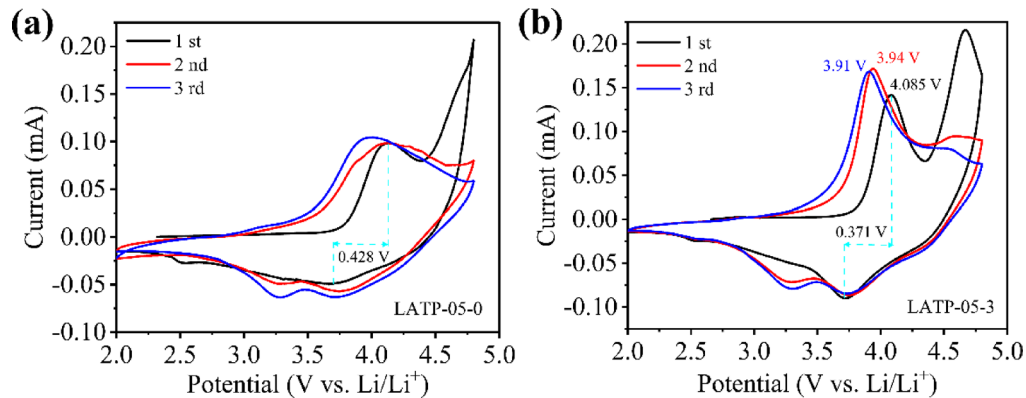


Fig. 7. (a) Initial charge–discharge curves, (b) charge–discharge curves after 10 cycles (c) rate performance curves, and (d) cyclic curves after 100 times at 0.1 C of LATP-05-X (X=0, 1, 1.5, 2, 3, 4).

charge and discharge curves after 10 charge and discharge cycles at 0.1 C are shown in Fig. 7(b). The LATP-05-1.5 sample still shows a discharge capacity of 218.3 $\text{mAh}\cdot\text{g}^{-1}$, which is much higher than the 180.2 $\text{mAh}\cdot\text{g}^{-1}$ of the LATP-05-0 sample. As the charge and discharge cycles proceed, the LATP-05-X (X=0, 1, 1.5, 2, 3, 4) materials are tested at rate. As shown in Fig. 7(c), with the increase of current density, the discharge performance of the LATP-05-3 sample gradually becomes prominent. At charge and discharge rates of 0.1 C, 0.2 C, 0.5 C, 1 C and

Cathode material	Capacity retention (%)
LATP-05-0	82.14
LATP-05-1	83.1
LATP-05-1.5	83.66
LATP-05-2	84.18
LATP-05-3	85.9
LATP-05-4	80.8

Table 3. The capacity retention of LATP-05-X (X=0, 1, 1.5, 2, 3, 4) after 100 cycles at 0.1 C.**Fig. 8.** CV curves of (a) LATP-05-0 and (b) LATP-05-3.

2 C, the specific discharge capacity of the LATP-05-3 electrode is $204.4 \text{ mAh}\cdot\text{g}^{-1}$, $177.2 \text{ mAh}\cdot\text{g}^{-1}$, $146.5 \text{ mAh}\cdot\text{g}^{-1}$, $121.1 \text{ mAh}\cdot\text{g}^{-1}$ and $96.4 \text{ mAh}\cdot\text{g}^{-1}$, respectively. When the current density is restored from 2 C to 0.1 C, the discharge specific capacity of the LATP-05-3 electrode is restored to $188.6 \text{ mAh}\cdot\text{g}^{-1}$, which is generally higher than other electrodes. In addition, after 100 cycles at 0.1 C, the capacity retention rate reached 85.9%, as shown in Fig. 7(d), and the optimal coating ratio of $\text{Li}_{1.5}\text{Al}_{0.5}\text{Ti}_{1.5}(\text{PO}_4)_3$ coating was 3%.

Table 3 compares the capacity retention of several cathode materials after 100 cycles. The results show that LATP-05-X (X=0, 1, 1.5, 2, 3, 4) materials have an electrochemical activation process. The first ten charge and discharge cycles in this chapter are all electrochemical activation processes of the materials, which are reflected in the rate diagram and cycle diagram. After the electrochemical activation, the charge and discharge performance of the materials tends to be stable. The $\text{Li}_{1.5}\text{Al}_{0.5}\text{Ti}_{1.5}(\text{PO}_4)_3$ coating provides high ionic conductivity, reduces the resistance of interfacial charge transfer, and realizes the release of high capacity of the material. At the same time, the coating effectively isolates the cathode material and the electrolyte, inhibits the corrosion of HF, and can effectively prevent the occurrence of side reactions at high current density and long cycle processes, stabilize the electrode surface structure, and reduce capacity loss. However, when the coating reaches a certain thickness, it will lead to the lengthening of the Li^+ diffusion path, which is not conducive to the deintercalation of Li^+ and weakens the electrochemical performance. After comparing Table S1, it can be seen that the $\text{Li}_{1.5}\text{Al}_{0.5}\text{Ti}_{1.5}(\text{PO}_4)_3$ -coated cathode material obtained excellent capacity retention while ensuring a superior level of discharge specific capacity.

The CV curves of the first three cycles of LATP-05-0 and LATP-05-3 materials are shown in Fig. 8(a, b). In the first cycle, the oxidation peak around 4.1 V corresponds to the removal of Li^+ and the oxidation of Ni^{2+} and Co^{3+} during the charging process of lithium-rich manganese-based materials, and the oxidation peak around 4.7 V corresponds to the activation of the Li_2MnO_3 phase and the removal of Li_2O to generate MnO_2 . The reduction peak near 3.62 V reflects the embedding of lithium ions in the layered lattice during the discharge process. It can be seen from the figure that the redox peaks of the first charge and discharge of LATP-05-0 and LATP-05-3 materials are significantly offset from the redox peaks of the second and third cycles, and the curves of the second and third cycles basically overlap, which is consistent with the intrinsic mechanism and typical characteristics of the charge and discharge of lithium-rich manganese-based materials. Comparing LATP-05-0 and LATP-05-3 materials, the oxidation peak intensity of LATP-05-0 decreased significantly in the second and third cycles, and the redox peak potential difference was 0.428 V, indicating that an irreversible phase change occurred inside the material; while the redox peak intensity of LATP-05-3 material remained basically unchanged in the three cycles, the redox peak current value was significantly greater than that of LATP-05-0, and the redox peak potential difference was 0.371 V, which was also significantly smaller than that of LATP-05-0, indicating that the dynamic performance was higher than that of LATP-05-0 material, the capacity loss was small in the first three cycles, and the good lithium ion insertion and extraction ability was conducive to the long cycle of the battery.

The lithium storage process of the battery material was characterized by the constant current intermittent titration (GITT) technique. The changes in the diffusion state of lithium ions in different voltage ranges were

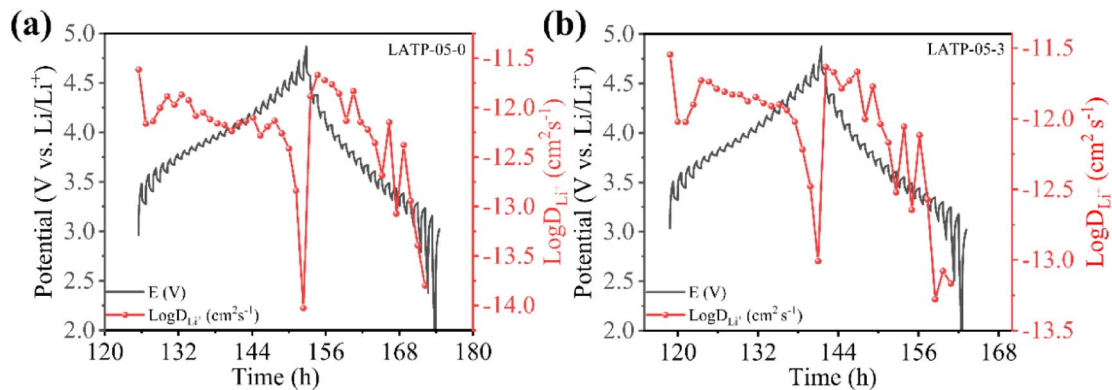


Fig. 9. (a, b) GITT test curve and lithium ion diffusion curve of LASO-0 and LASO-3 materials, respectively.

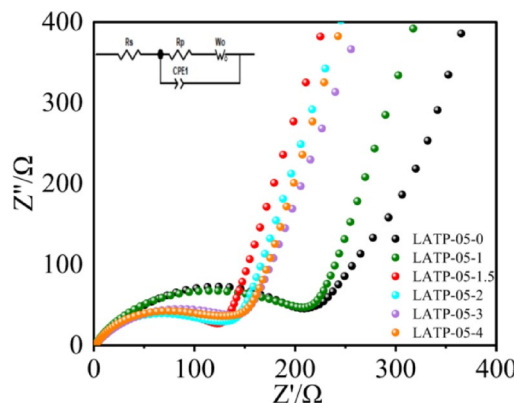


Fig. 10. AC impedance spectra of the LATP-05-X (X=0, 1, 1.5, 2, 3, 4) materials.

tested, and the lithium insertion and extraction processes of the materials were analyzed. In the GITT test, the LATP-05-0 and LATP-05-3 materials were charged at a current density of 0.1 C for 30 min in the voltage range of 2.0~4.8 V, and the battery voltage was allowed to recover to a stable value for 40 min under the open circuit voltage state. This process was repeated until the high cutoff voltage (4.8 V), and the same discharge process was continued until the low cutoff voltage (2 V). Figure 9(a, b) reflects the diffusion of lithium ions during the complete charge and discharge process of LATP-05-0 and LATP-05-3 materials, respectively, and the change trend of lithium ion diffusion is the same. In the charge and discharge stages, the LogD_{Li⁺} values of the LATP-05-3 material at different voltages are higher than those of the LATP-05-0 material. This further proves that the LATP-05-3 material has higher electronic/ionic conductivity and better interface stability, thus showing excellent electrochemical performance.

Figure 10 is the AC impedance curve of LATP-05-X (X=0, 1, 1.5, 2, 3, 4) materials. It can be observed that the charge transfer impedance of LATP-05-3 electrode at low frequency and the ion diffusion impedance at high frequency are significantly smaller than those of LATP-05-0 electrode material, and LATP-05-3 electrode also shows the smallest charge transfer impedance among the six materials with different proportions. The surface LATP-05-3 material has a wide internal lithium ion migration channel and a fast ion deintercalation rate. This may be due to the fact that the particle size of LATP-05-3 material after coating modification becomes smaller and more uniform, and the surface area increases, which promotes charge transfer and ion diffusion.

In order to further study the ion dynamics process inside the LATP-05-3 material, Fig. 11 shows the CV results of LATP-05-3 at scan rates of 0.2, 0.5, 0.7, and 1 mV·s⁻¹ and the impedance of the electrode after 100 cycles at 0.1 C. In Fig. 11(a), with the increase in the scan rate, the displacement of the oxidation peak and reduction peak of LATP-05-3 did not change significantly, the peak intensity increased and maintained a good peak shape, indicating that the degree of redox reaction inside the electrode material increased, which can reflect the strong deintercalation ability of lithium ions inside the material, indicating that there is a small electrochemical polarization problem in the LATP-05-3 material, with good electrochemical reversibility, and good matching of lithium ion migration and electron transfer speed. In Fig. 11(b), the charge transfer impedance decreases after cycling. We can analyze that the electrode material has an activation process during the charge and discharge test. When the electrode is not fully activated, the voltage and charge and discharge specific capacity are in an unstable state, and the impedance value is naturally larger. As the cycle progresses, the active substance is activated, the impedance decreases, and the stability of the electrode material is enhanced.

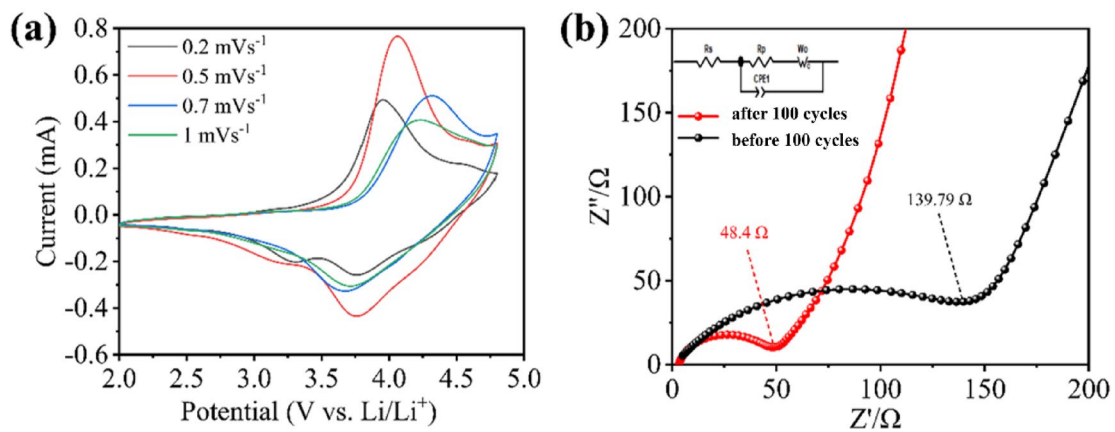


Fig. 11. (a) Cyclic voltammery results at different sweep speeds; (b) Ac impedance spectrum after 100 cycles at 0.1 C of LATP-05-3.

4. Conclusion

In this paper, the fast ion conductor $\text{Li}_{1.5}\text{Al}_{0.5}\text{Ti}_{1.5}(\text{PO}_4)_3$ with three-dimensional lithium ion channels was coated on the surface of $\text{Li}_{1.2}\text{Mn}_{0.54}\text{Ni}_{0.13}\text{Co}_{0.13}\text{O}_2$ by sol-gel method and high temperature calcination method, and the modified positive electrode material was applied to lithium ion batteries to test its electrochemical performance. The experimental results show that the $\text{Li}_{1.2}\text{Mn}_{0.54}\text{Ni}_{0.13}\text{Co}_{0.13}\text{O}_2@\text{Li}_{1.5}\text{Al}_{0.5}\text{Ti}_{1.5}(\text{PO}_4)_3$ composite material with a coating amount of 3% has the highest capacity retention rate after 100 cycles. The presence of $\text{Li}_{1.5}\text{Al}_{0.5}\text{Ti}_{1.5}(\text{PO}_4)_3$ on the surface of $\text{Li}_{1.2}\text{Mn}_{0.54}\text{Ni}_{0.13}\text{Co}_{0.13}\text{O}_2$ was confirmed by XRD characteristic peaks, element percentage in EDS, and binding energy in XPS spectra. By comparing the first charge and discharge curves of the six samples, it was found that the initial discharge capacity of the LATP-05-1.5 sample was the highest, reaching $219 \text{ mAh}\cdot\text{g}^{-1}$, and the initial coulombic efficiency was as high as 71.29%. As the charge and discharge cycles proceeded, it was found that all materials underwent an activation process. After activation, the final LATP-05-3 sample had the best cycle stability. After 100 cycles at 0.1 C, the capacity retention rate reached 85.9%, which was better than the 82.14% of the base material. In the cyclic voltammetry test, the redox potential difference of LATP-05-3 is 0.371 V, and the charge transfer impedance value is the smallest among several materials. The GITT test proves that the LATP-05-3 material has a higher ion diffusion coefficient and a higher lithium ion deintercalation rate. In summary, the lithium fast ion conductor $\text{Li}_{1.5}\text{Al}_{0.5}\text{Ti}_{1.5}(\text{PO}_4)_3$ is coated on the surface of $\text{Li}_{1.2}\text{Mn}_{0.54}\text{Ni}_{0.13}\text{Co}_{0.13}\text{O}_2$, which protects the electrode from HF corrosion while reducing the internal ion migration resistance of the material, so that the LATP-05-3 composite material exhibits the best ion diffusion state.

Data availability

The authors confirm that the data supporting the findings of this study are available within the article.

Received: 9 September 2024; Accepted: 9 July 2025

Published online: 18 July 2025

References

- Wang, D., Li, G. X. & Pan, Y. L. Application of lithium-ion battery technology in space field. *Shanghai Aerosp.* **1** (5), 54–58. <https://doi.org/10.3969/j.issn.1006-1630.2000.01.011> (2000).
- Cai, Z. H., Huang, Y., Zhu, W. C. & Xiao, R. G. Increase in ionic conductivity of NASICON-type solid electrolyte $\text{Li}_{1.5}\text{Al}_{0.5}\text{Ti}_{1.5}(\text{PO}_4)_3$ by Nb_2O_5 doping. *Solid State Ionics* **354**, 115399. <https://doi.org/10.1016/j.ssi.2020.115399> (2020).
- Zhang, S. S. Liquid electrolyte lithium/sulfur battery: fundamental chemistry, problems, and solutions. *J. Power Sources* **231** (1), 153–162. <https://doi.org/10.1016/j.jpowsour.2012.12.102> (2013).
- Dunn, B., Kamath, H. & Tarascon, J. M. Electrical energy storage for the grid: A battery of Choices. *Science* **334** (6058), 928–935. <https://doi.org/10.1126/science.1212741> (2011).
- Fergus, J. W. Recent developments in cathode materials for lithium ion batteries. *J. Power Sources* **195** (4), 939–954. <https://doi.org/10.1016/j.jpowsour.2009.08.089> (2010).
- An, F. Q., Zhao, H. L., Qiu, J., C. Z., Zhou, Y. C. & Li, W. N. Development status and research progress of lithium-ion batteries for pure electric vehicles. *Chin. J. Eng. Sci.* **41** (1), 22–42. <https://doi.org/10.13374/j.issn2095-9389.2019.01.003> (2019).
- Feng, X. et al. Enhanced electrochemical performance of Ti-doped $\text{Li}_{1.2}\text{Mn}_{0.54}\text{Co}_{0.13}\text{Ni}_{0.13}\text{O}_2$ for lithium-ion batteries. *J. Power Sources* **317** (15), 74–80. <https://doi.org/10.1016/j.jpowsour.2016.03.101> (2016).
- He, P., Yu, H. J. & Li, D. Layered lithium transition metal oxide cathodes towards high energy lithium-ion batteries. *J. Mater. Chem.* **22** (9), 3680–3695. <https://doi.org/10.1039/c2jm14305d> (2012).
- Yabuuchi, N., Yoshii, K., Myung, S. T., Nakai, I. & Komaba, S. Detailed studies of a High-Capacity electrode material for rechargeable batteries, $\text{Li}_2\text{MnO}_3-\text{LiCo}_{1/3}\text{Ni}_{1/3}\text{Mn}_{1/3}\text{O}_2$. *J. Am. Chem. Soc.* <https://doi.org/10.1021/ja108588y> (2011).
- Yang, H., Liu, H. & Wang, Y. B. Calcareous tube-worm fossils in microbialites after end-Permian mass extinction and their paleoenvironmental implications. *J. Earth Sci.* <https://doi.org/10.1007/s12583-010-0203-0> (2010).
- Wen, L. et al. Improved electrochemical performance of LaF_3 -coated layered oxide $\text{Li}_{1.2}\text{Mn}_{0.54}\text{Ni}_{0.13}\text{Co}_{0.13}\text{O}_2$ cathode material for lithium-ion batteries prepared by sol-gel method. *Int. J. Electrochem. Sci.* **16**, 210344. <https://doi.org/10.20964/2021.03.74> (2021).

12. Shu, W., Jian, Z., Zhou, J., Zheng, Y. & Chen, W. Boosting the electrochemical performance of $\text{Li}_{1.2}\text{Mn}_{0.54}\text{Ni}_{0.13}\text{Co}_{0.13}\text{O}_2$ by rough coating with the superionic conductor $\text{Li}_7\text{La}_3\text{Zr}_2\text{O}_{12}$. *ACS Appl. Mater. Interfaces* **46** (13), 54916–54923. <https://doi.org/10.1021/acsami.1c14229> (2021).
13. Zhai, X. H., Zhang, P. P. & Huang, H. Surface grafting SiO_2 on lithium-rich layered oxide cathode material for improving structural stability. *J. Electrochem. Soc.* **168** (6), 1–13. <https://doi.org/10.1149/1945-7111/ac0948> (2021).
14. He, L. et al. SmPO_4 -coated $\text{Li}_{1.2}\text{Mn}_{0.54}\text{Ni}_{0.13}\text{Co}_{0.13}\text{O}_2$ as a cathode material with enhanced cycling stability for lithium ion batteries. *Ceram. Int.* **43** (6), 5267–5273. <https://doi.org/10.1016/j.ceramint.2017.01.052> (2017).
15. Shang, K. H., He, W., Ai, X. P., Cao, Y. L. & Yang, H. X. Study on amorphous borophosphorous glass coated with $\text{Li}_{1.2}\text{Co}_{0.13}\text{Ni}_{0.13}\text{Mn}_{0.54}\text{O}_2$ cathode material. *Power Supply Technol.* **40** (2), 5. <https://doi.org/10.3969/j.issn.1002-087X.2016.02.005> (2016).
16. Chen, Y. X., Li, Y. J., Chang, S. H., Wang, S. L. & Li, W. Epoxy-functionalized silane grafting enhances the cycling performances of $\text{Li}_{1.2}\text{Mn}_{0.54}\text{Ni}_{0.13}\text{Co}_{0.13}\text{O}_2$ cathode materials. *J. Ionics* **26** (8), 3761–3768. <https://doi.org/10.1007/s11581-020-03561-1> (2020).
17. Song, C. K., Feng, W. J., Shi, Z. J. & Huang, Z. Y. Coating TiO_2 on lithium-rich $\text{Li}_{1.2}\text{Mn}_{0.54}\text{Ni}_{0.13}\text{Co}_{0.13}\text{O}_2$ material to improve its electrochemical performance. *J. Ionics* 1–12. <https://doi.org/10.1007/s11581-020-03854-5> (2020).
18. Cao, J. et al. Enhance electrochemical performances of $\text{Li}_{1.2}\text{Mn}_{0.54}\text{Ni}_{0.13}\text{Co}_{0.13}\text{O}_2$ cathode material coated with ZrO_2 . *Ionics* **29**, 51–60. <https://doi.org/10.1007/s11581-022-04828-5> (2023).
19. Yu, H., He, X. Q. & Liang, X. H. $\text{AlF}_3\text{-Al}_2\text{O}_3$ ALD thin-film-coated $\text{Li}_{1.2}\text{Mn}_{0.54}\text{Ni}_{0.13}\text{Co}_{0.13}\text{O}_2$ particles for lithium-ion batteries: long-term protection. *ACS Appl. Mater. Interfaces* **14** (3), 3991–4003. <https://doi.org/10.1021/acsami.1c20005> (2022).
20. Yang, Q. et al. Surface-protected LiCoO_2 with ultrathin solid oxide electrolyte film for high-voltage lithium ion batteries and lithium polymer batteries. *J. Power Sources* **388**, 65–70. <https://doi.org/10.1016/j.jpowsour.2018.03.076> (2018).
21. Maldonado-Manso, P., Losilla, E. R. & Martínez-Lara, J. High Lithium Ionic Conductivity in the $\text{Li}_{1+x}\text{Al}_x\text{GeyTi}_{2-x-y}(\text{PO}_4)_3$ NASICON Series. *J. Mat. Sci.* **15** (9), 1879–1885. <https://doi.org/10.1021/cm021717j> (2003).
22. Zhang, B. Z. Research progress and prospect of perovskite lithium fast ion conductor. *J. Jinz. Univer.* **24** (3), 4 <https://doi.org/CNKI:SUN:JGZK.0.2007-03-007> (2007).
23. Lee, J. W. Improved electrochemical properties of $\text{Li}(\text{Ni}_{0.6}\text{Mn}_{0.2}\text{Co}_{0.2})\text{O}_2$ by surface coating with $\text{Li}_{1.3}\text{Al}_{0.3}\text{Ti}_{1.7}(\text{PO}_4)_3$. *J. Power Sources* <https://doi.org/10.1016/j.jpowsour.2015.12.055> (2016).
24. Liang, J. Y. et al. Mitigating interfacial potential drop of Cathode-Solid electrolyte via ionic conductor layer to enhance interface dynamics for solid Batteries. *J. Am. Chem. Soc.* **140** (22), 6767–6770. <https://doi.org/10.1021/jacs.8b03319> (2018).
25. Wu, X. M., Li, R. X., He, Z. Q. & Chen, S. Synthesis and characterization of $\text{Li}_{1.3}\text{Al}_{0.3}\text{Ti}_{1.7}(\text{PO}_4)_3$ -coated LiMn_2O_4 by wet chemical route. *Rare Met.* **28**, 122–126. <https://doi.org/10.1007/s12598-009-0024-4> (2009).
26. Wang, Y. et al. Improved electrochemical performance of $\text{Li}(\text{Ni}_{0.6}\text{Co}_{0.2}\text{Mn}_{0.2})\text{O}_2$ at high charging cut-off voltage with $\text{Li}_{1.4}\text{Al}_{0.4}\text{Ti}_{1.6}(\text{PO}_4)_3$ surface coating. *Chin. Phys. B* **28** (6), 068202. <https://doi.org/10.1088/1674-1056/28/6/068202> (2019).
27. Zhang, N., Li, Y., Luo, Y. D., Yang, Z. & Lu, J. Y. Impact of $\text{LiTi}_2(\text{PO}_4)_3$ coating on the electrochemical performance of $\text{Li}_{1.2}\text{Mn}_{0.54}\text{Ni}_{0.13}\text{Co}_{0.13}\text{O}_2$ using a wet chemical method. *Ionics* **27** (4), 1465–1475. <https://doi.org/10.1007/s11581-021-03946-w> (2021).

Acknowledgements

This research was supported by the Research Program of Application Foundation of Qinghai Province (No. 2024-ZJ-787).

Author contributions

S.-M. Yang and S.-P Shao wrote the main manuscript text. Yu-Long Xie: Funding acquisition, Project administration, Resources, Supervision, Writing - review editing. All authors reviewed the manuscript.

Declarations

Competing interests

The authors declare no competing interests.

Additional information

Supplementary Information The online version contains supplementary material available at <https://doi.org/10.1038/s41598-025-11331-0>.

Correspondence and requests for materials should be addressed to Y.-L.X.

Reprints and permissions information is available at www.nature.com/reprints.

Publisher's note Springer Nature remains neutral with regard to jurisdictional claims in published maps and institutional affiliations.

Open Access This article is licensed under a Creative Commons Attribution-NonCommercial-NoDerivatives 4.0 International License, which permits any non-commercial use, sharing, distribution and reproduction in any medium or format, as long as you give appropriate credit to the original author(s) and the source, provide a link to the Creative Commons licence, and indicate if you modified the licensed material. You do not have permission under this licence to share adapted material derived from this article or parts of it. The images or other third party material in this article are included in the article's Creative Commons licence, unless indicated otherwise in a credit line to the material. If material is not included in the article's Creative Commons licence and your intended use is not permitted by statutory regulation or exceeds the permitted use, you will need to obtain permission directly from the copyright holder. To view a copy of this licence, visit <http://creativecommons.org/licenses/by-nc-nd/4.0/>.

© The Author(s) 2025